

Nonlocality of local Andreev conductances as a probe for topological Majorana wires

Rodrigo A. Dourado,¹ Poliana H. Penteado,¹ and J. Carlos Egues^{1,2}

¹*Instituto de Física de São Carlos, Universidade de São Paulo, 13560-970 São Carlos, São Paulo, Brazil*

²*Department of Physics, University of Basel, Klingelbergstrasse 82, CH-4056 Basel, Switzerland*

Identifying topological phases via zero-bias conductance peaks in Majorana wires is not trivial. Here we address this issue in realistic three-terminal proximitized superconducting (disordered) nanowires coupled to normal leads, purportedly capable of hosting (quasi-) zero-energy Majorana modes. By using Green functions and the scattering matrix formalism, we calculate the conductance matrix and the local density of states (LDOS) for asymmetrically tunnel coupled left (Γ_L , constant) and right (Γ_R) leads. In the trivial phase, we find that the local conductances are distinctively affected by variations in Γ_R : while G_{LL} is essentially constant, G_{RR} is exponentially suppressed as Γ_R diminishes. In the topological phase (bulk criterion), surprisingly, G_{LL} and G_{RR} are suppressed in the exact same way, i.e., $G_{LL} = G_{RR}$. This nonlocal suppression of G_{LL} scales with the hybridization between the Majorana zero modes (MZMs) and arises from the emergence of a dip in the LDOS around zero energy at the left end of the wire, which in turn affects the MZM-mediated local Andreev reflections. We also present a Majorana transistor exploiting the nonlocality of the local Andreev processes and the gate-controlled suppression of the LDOS. Finally we propose a protocol for distinguishing trivial from topological zero-bias peaks that rely only on local conductance measurements.

Introduction.— Semiconducting nanowires with proximity-induced superconductivity, in principle capable of hosting Majorana zero modes (MZMs) [1], have become a paradigmatic system to investigate topological matter. Following theoretical predictions [2, 3], some of the early experiments [4–6] relied on observing zero-bias (local) conductance peaks as the primary signature of MZMs. However, it was soon realized that these zero-bias peaks (ZBPs) could also arise from other mechanisms, e.g., the Kondo effect, disorder, and Andreev bound states [7]. Despite advances in materials and device optimization in the past decade, there is still no clear-cut experimental evidence of MZMs in these systems.

A concrete step towards changing the above scenario was taken by Microsoft Quantum, which proposed [8] and implemented [9] a protocol to identify topological phases in hybrid semiconductor-superconductor three-terminal devices. This protocol relies on the observation of coexisting ZBPs in the local conductance on the left (G_{LL}) and right (G_{RR}) ends of the nanowire and a closing and re-opening of the bulk transport gap as measured in the nonlocal conductance (G_{LR}) [10]. Interestingly in Ref. [11], the authors show that trivial mechanisms can mimic similar features of the topological gap protocol.

In this work, we consider realistic three-terminal semiconductor-superconductor wires, Fig. 1, similar to those in Refs. [8–10, 12, 13]. Unlike previous works [8–10], however, here we propose only the zero-bias local conductances G_{LL} and G_{RR} as sufficient probes to tell apart trivial and topological phases; here we use the bulk criterion ($V_z = \sqrt{\mu^2 + \Delta^2}$, with V_z the Zeeman energy, μ the superconductor chemical potential, and Δ the proximity-induced superconducting gap) to define the topological quantum phase transition. Our proposal exploits a peculiar nonlocality of dominant *local* Andreev

reflection (LAR) processes in the topological phase; comparatively, direct tunneling and crossed Andreev reflection (CAR) are negligible in the parameter range investigated, see SM [14] for details [e.g., Fig. S1 (b)]. These retroreflections involve an incoming electron and an outgoing hole with either opposite (usual LAR) or same (spin-selective LAR [15]) spins, Fig. 2 (a). We use the scattering matrix and Green function approaches to obtain the conductance matrix and the LDOS for generic asymmetric couplings Γ_L and Γ_R , which can be tuned via the barriers U_L and U_R , respectively, Fig. 1 (a).

Pristine nanowires.— Interestingly, as we increase the ratio U_R/U_L , we find that for single-subband nanowires with no disorder or nonuniformities (i) $G_{LL} = G_{RR}$, decreasing monotonically in the topological phase [solid blue lines in Figs. 1 (b) and (c)] while (ii) in the trivial phase G_{LL} is constant and G_{RR} is exponentially suppressed [dashed blue lines in Figs. 1 (b) and (c)].

The *nonlocal* behavior of G_{LL} in the topological regime arises from the suppression of LAR processes at the *left* end of the wire, Fig. 2 (a). This follows from the LDOS developing a zero-energy nonlocal dip at this same left end as the *right* barrier U_R is raised, Fig. 3 (a) [note the corresponding suppression in G_{LL} , inset Fig. 3 (b)]. This potential height increase also suppresses G_{RR} , even though the LDOS at the right side is actually enhanced. Here the spin-selective LAR [15], whose reflection probability is $A_{\sigma\sigma'}^\alpha$ ($\alpha = L, R$), is the dominant process, Fig. 2 (b). In fact, in the pristine case, all LAR probabilities $A_{\sigma\sigma'}^\alpha$ are mediated by (quasi-) zero-energy modes with $A_L = A_R$, where $A_\alpha = \sum_{\sigma,\sigma'} A_{\sigma\sigma'}^\alpha$. In the trivial regime, on the other hand, the usual LAR $A_{\sigma\bar{\sigma}}^\alpha$ with opposite spins $\sigma, \bar{\sigma}$ is the only nonzero contribution [16]. In this case, $A_{\sigma\bar{\sigma}}^L$ remains constant while $A_{\sigma\bar{\sigma}}^R$ exponentially goes to zero as U_R/U_L is increased (U_L is kept constant).

Disordered/nonuniform nanowires.—We also investi-

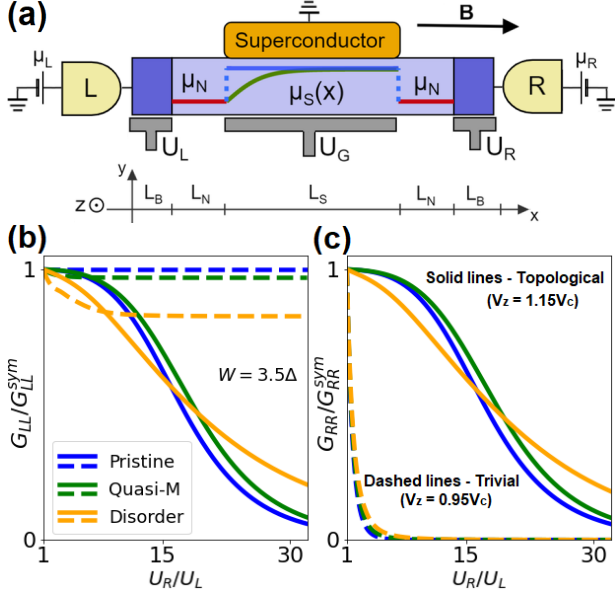


FIG. 1. (a) Semiconductor-superconductor Rashba nanowire (purple) with a magnetic field \mathbf{B} along the x axis coupled to left (L) and right (R) normal leads, via the gates U_L and U_R , respectively. The chemical potentials of the leads μ_L and μ_R are measured with respect to the grounded parent superconductor (orange). The chemical potential $\mu_S(x)$ and μ_N refer to the superconducting and normal parts of the nanowire, respectively. (b) G_{LL} and (c) G_{RR} as functions of U_R/U_L . The solid and dashed lines in (b) and (c) denote the topological and trivial phases, respectively. For either of these phases we consider the “pristine” (clean wire, $\mu_S(x) = \mu$), “quasi-Majorana” (nonuniform $\mu_S(x)$ profile) and disordered scenarios. In the topological regime, for any of these cases, $G_{LL} = G_{RR}$ is suppressed as U_R/U_L increases. In the trivial regime, G_{LL} remains essentially constant (the disordered case shows a small initial suppression), while G_{RR} is exponentially suppressed. This unique behavior of G_{LL} and G_{RR} highlights a nonlocality of LAR that allows one to tell apart topological and trivial phases. Realistic parameters used (in units of meV): $t = \hbar^2/2m^*a^2 = 102$, $\mu = 1$, $\mu_N = 0.2$, $\Delta = 0.5$, $\alpha = \alpha_R/2a = 3.5$, with $a = 5$ nm [12], and $U_L = 5$. The lengths are (in units of μm) $L_S = 2.5$, $L_N = 0.1$, and $L_B = 0.02$. In (a) $U_R = 5$.

gate the effects of disorder and nonuniform chemical potential profiles (“quasi-Majoranas”), Fig. 1. Quite surprisingly, even in these regimes G_{LL} and G_{RR} behave like the pristine case as a function of U_R/U_L , see Figs. 1 (b) and (c). Moreover, we have verified that the conductances shown in Figs. 1 and 2 are stable against variations of, e.g., the applied magnetic field \mathbf{B} [see Figs. 2 (b) and (c)], the wire carrier density, the barrier transparency, and the wire length (not shown). Hence we contend that by measuring only G_{LL} and G_{RR} versus U_R/U_L , one can distinguish the trivial ($G_{LL} \neq G_{RR}$) and topological ($G_{LL} = G_{RR}$) phases. In passing, we note that for true MZMs (i.e., with exactly zero energy) $G_{LL} = G_{RR}$ displays a plateau at $2e^2/h$ as a function of U_R/U_L . All

our results are symmetric with respect to exchanging U_R by U_L and vice-versa. As an application, we propose a Majorana-QD-based transistor exploiting the nonlocality of the LAR processes and the gate-tunable suppression of the LDOS around zero energy, Fig. 4.

We note that nonlocal effects manifested in G_{LL} were first investigated in connection with the thermal conductance in the regime $\Gamma_L \approx \Gamma_R$, focusing on $\delta\Gamma_R/\Gamma_R \ll 1$ [17, 18]. In this perturbative limit, $\delta G_{LL} = G_{LL}(\Gamma_R + \delta\Gamma_R, \Gamma_L) - G_{LL}(\Gamma_R, \Gamma_L)$ contains (in lowest order in $\delta\Gamma_R$) only direct tunneling and CAR contributions. In our work, however, we consider a nonperturbative regime, in which $\delta G_{LL} \approx G_{LL}$ is dominated by LAR terms.

Model Hamiltonian.— In the Nambu basis $\Psi(x) = \{\psi_{\uparrow}(x), \psi_{\downarrow}(x), \psi_{\uparrow}^{\dagger}(x), -\psi_{\uparrow}^{\dagger}(x)\}^T$, with $\psi_{\sigma}(x)$ the electron field operator for spin σ at position x , the nanowire is modeled by [2, 3]

$$H_{\text{NW}} = \frac{1}{2} \sum_{\sigma} \int dx \Psi^{\dagger}(x) \left[\left(\frac{\hbar^2 \partial_x^2}{2m^*} - i\alpha_R \partial_x \sigma_y - \mu_S(x) \right) \tau_z + V_z \sigma_x + \Delta \tau_x \right] \Psi(x), \quad (1)$$

where m^* is the effective mass of the electron, α_R the Rashba spin-orbit coefficient, μ_S the chemical potential, V_z the Zeeman energy, Δ the proximity-induced superconducting gap, and σ_i and τ_i the Pauli matrices acting on the spin and particle-hole subspaces, respectively. We assume a weak coupling between the wire and the SC [19], which possibly mitigates the suppression of the topological gap [20] and the metallization of the nanowire [21].

Our nanowire also contains two outer barriers (L_B , μ_B) followed by normal regions (L_N , μ_N), with $\mu_B = \mu_N - U_{L,R}$, and $\Delta = V_z = 0$. The central region, described by Hamiltonian (1), has length L_S , Fig. 1 (a). The system is coupled to L and R metallic leads at chemical potentials μ_L and μ_R , respectively, with respect to the grounded SC. We consider three different scenarios: (i) $\mu_S(x) = \mu$, uniform (“pristine wire”), (ii) $\mu_S(x) = \mu_N + (\mu - \mu_N) \tanh[(x - L_S)/\lambda]$, a “confining potential” on the left side of the wire such that $\lambda = 0.16L_S$ controls the smoothness of the transition $\mu_N \rightarrow \mu$. Near-zero energy states called quasi-Majoranas emerge for $V_z < V_c = \sqrt{\mu^2 + \Delta^2}$, confined in the potential region [22, 23], (iii) $\mu_S(x) = \mu - V_{dis}(x)$, Anderson-type on-site disorder potential $V_{dis}(x)$ with values randomly taken from the interval $[-W, W]$. We use (i) exact numerical diagonalization to obtain the spectrum and wave functions of the Bogoliubov de-Gennes Hamiltonian, and (ii) the package KWANT [24] to calculate the Andreev probabilities $A_{\sigma\sigma'}^{\alpha}$ and the conductance coefficients $G_{\alpha\beta}$.

Topological Andreev bound states.— In the trivial phase, and in particular for $V_z \ll m^* \alpha_R^2/\hbar^2$, electrons are reflected as holes of opposite spin with probability

$A_{\uparrow\downarrow}^\alpha$ [16]. In contrast, the topological phase ($V_z > V_c$) is characterized by the emergence of same-spin LAR processes $A_{\uparrow\uparrow}^\alpha$ and $A_{\downarrow\downarrow}^\alpha$, in addition to opposite-spin LAR $A_{\uparrow\downarrow}^\alpha$. Here, we will refer to these modes as topological Andreev bound states (ABS), because they arise from the hybridization of true Majorana zero modes. The eigenenergies of these quasi-degenerate states are entirely due to this hybridization [25], as opposed to ordinary ABSs, whose energies are mostly due to confinement. The probabilities $A_{\uparrow\uparrow}^\alpha$ and $A_{\downarrow\downarrow}^\alpha$ are in principle measurable via polarized leads [15] or spin-selective QDs [26].

In Fig. 2 (a), for, e.g., $U_L = U_R$, we show $A_{\sigma\sigma'}^L$, as functions of V_z for opposite-spin LAR (blue curves) and same-spin LAR (grey curves); a similar plot holds for $A_{\sigma\sigma'}^R$. Even though the individual LAR components are distinct, $A_{\sigma\sigma'}^L \neq A_{\sigma\sigma'}^R$, the total LAR probability A_α ($A_\alpha = \sum_{\sigma\sigma'} A_{\sigma\sigma'}^\alpha$) is equal on both ends of the pristine wire, $A_L = A_R$. To see that the dominant same-spin LAR processes are directly related to topological ABSs (i.e., split Majorana states), let us consider the strictly $E = 0$ case (true Majoranas). For simplicity, we consider the L lead and the SC as forming an NS junction, whose LAR matrix in zeroth order in the Rashba coupling ($2m^*\alpha_R^2/h^2 \ll \sqrt{V_z^2 - \Delta^2}$) and for $V_z > V_c$ is [15]

$$r^{he}(V_z) = \begin{pmatrix} r_{\uparrow\uparrow}^{he} & r_{\uparrow\downarrow}^{he} \\ r_{\downarrow\uparrow}^{he} & r_{\downarrow\downarrow}^{he} \end{pmatrix} = \begin{pmatrix} \frac{V_z - \sqrt{V_z^2 - \Delta^2}}{2V_z} & -\frac{\Delta}{2V_z} \\ -\frac{\Delta}{2V_z} & \frac{V_z + \sqrt{V_z^2 - \Delta^2}}{2V_z} \end{pmatrix}. \quad (2)$$

Within this approximation, $A_{\downarrow\downarrow}^L \approx |r_{\downarrow\downarrow}^{he}|^2 \approx 1 - \Delta^2/2V_z^2$, $A_{\uparrow\uparrow}^L \approx |r_{\uparrow\uparrow}^{he}|^2 \approx \Delta^4/16V_z^4$, $A_{\uparrow\downarrow}^L = A_{\downarrow\uparrow}^L \approx |r_{\uparrow\downarrow}^{he}|^2 \approx \Delta^2/4V_z^2$, and $A_L \approx 1$ (up to $O(\Delta/V_z)^2$), which qualitatively describe the behavior shown in Fig. 2 (a) [27]. Note that $A_{\downarrow\downarrow}^L$ oscillates as V_z increases, exhibiting a dip at $V_z \approx 1.5V_c$; at this point, direct tunneling and CAR processes are favoured [14, 28]. This oscillating behavior follows from the lowest topological ABS pair crossing at $E = 0$ as V_z varies (Majorana oscillations) [29–31].

Nonlocality of local Andreev reflection.— In the topological phase, the LAR processes on both sides of the wire are sensitive to the increase of U_R/U_L , as shown in Fig. 2 (b), in which we choose $V_z = 1.15V_c$ [dotted vertical line in Fig. 2 (a)], $U_L = 5$, and vary U_R . As the right barrier U_R increases, the left LAR probability $A_{\sigma\sigma'}^L$ decreases. This nonlocal feature of the local Andreev process arises from the topological ABSs. Similarly, the right LAR probability $A_{\sigma\sigma'}^R$ is nonlocal for variations of the left barrier U_L .

Local conductance.— At zero bias, the local conductance reads $G_{\alpha\alpha} = \frac{2e^2}{h}(2A_\alpha + T_{\bar{\alpha}\alpha} + A_{\bar{\alpha}\alpha})$, where $T_{\bar{\alpha}\alpha}$ and $A_{\bar{\alpha}\alpha}$ are the probabilities of an incoming electron in lead $\alpha = L$ (R) to be transmitted as an electron or as a hole, respectively, to lead $\bar{\alpha} = R$ (L). In Figs. 2 (c) and (d), we show, respectively, G_{LL} and G_{RR} as functions of U_R/U_L in the topological phase for $V_z = 1.15V_c$ (orange

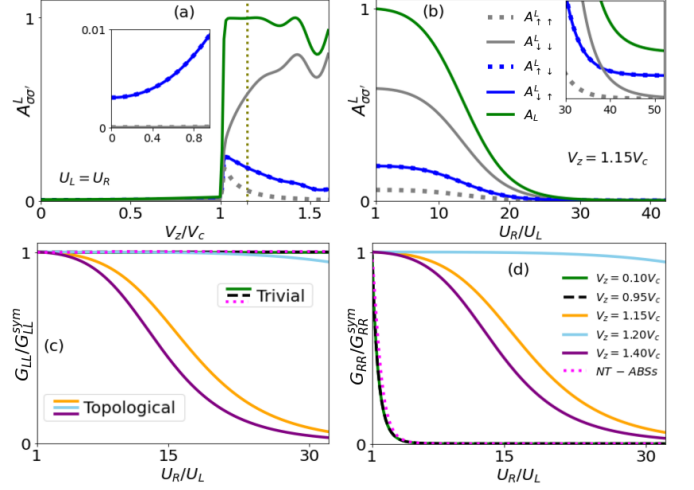


FIG. 2. Local Andreev reflection probabilities $A_{\sigma\sigma'}^L$, and local conductances G_{LL} and G_{RR} in the pristine wire. (a) $A_{\sigma\sigma'}^L$ as a function of the Zeeman field. The topological phase is followed by the rapid increase of $A_{\uparrow\uparrow}^L$ and $A_{\downarrow\downarrow}^L$ in grey. (b) $A_{\sigma\sigma'}^L$ as a function of U_R/U_L in the topological phase, $V_z = 1.15V_c$ [vertical dotted line in (a)]. We observe a suppression of the LAR components as U_R/U_L increases. (c) G_{LL} and (d) G_{RR} as functions of U_R/U_L . For $V_z > V_c$ (orange, cyan, and purple curves), $G_{LL} = G_{RR}$ is suppressed as U_R/U_L increases. For $V_z < V_c$ (green and black curves) and for fine-tuned ABSs in a nontopological (NT) wire (magenta curve), i.e., $\alpha = V_z = 0$ in the superconducting region of the wire, G_{LL} remains constant while G_{RR} is exponentially suppressed due to the tunnel barrier height. The parameters used here are the same as those in Fig. 1. For the NT case we consider $\alpha = 0$, $V_z = 1.16V_c$ and $\mu_N = 2.58$, the other parameters remain the same.

curve), $V_z = 1.20V_c$ (cyan), and $V_z = 1.40V_c$ (purple). We observe that they are both equally suppressed following the nonlocal behavior of $A_L = A_R$ in Fig. 2 (b). The hybridization between the MZMs on the left and right sides of the wire is responsible for this nonlocality. Hence the $G_{LL} = G_{RR}$ suppression is more prominent for $V_z = 1.15V_c$ and $V_z = 1.40V_c$ as compared to $V_z = 1.20V_c$ since $\varepsilon_m(V_z = 1.40V_c) > \varepsilon_m(V_z = 1.15V_c) >> \varepsilon_m(V_z = 1.20V_c)$, where ε_m is the energy of the lowest topological ABS mode. For the cyan curve, we choose V_z near a parity crossing point of the topological ABSs, such that their energy ε_m is close to zero (see, e.g., Fig. S1 in the SM [14]). In this case, the dependence on U_R is noticeable only for $U_R/U_L \sim 30$. In the limit $\varepsilon_m \rightarrow 0$, we regain $G_{LL} = G_{RR} = 2e^2/h$, i.e., the quantized strictly zero-energy Majorana conductance.

In the trivial phase, $V_z = 0.10V_c$ (green curve) and $V_z = 0.95V_c$ (dashed black line), G_{LL} does not have any dependence on U_R , while G_{RR} exponentially decreases when the tunnel barrier height increases, in agreement with Ref. [32] for an s-wave SC. These results remain valid as long as $L_S >> \xi$, with ξ the localization length of the superconductor [33], when LAR is the dominant process. Interestingly, we observe a crossing point where $A_{\downarrow\downarrow}^L$

drops below $A_{\downarrow\downarrow}^L = A_{\uparrow\uparrow}^L$ [see inset of Fig 2 (b)]. The latter reaches a plateau for larger U_R values, indicating a residual contribution from usual, as opposed to the (quasi-) zero-energy-mediated LAR. In Figs. 1 (b), (c), and 2 (c), (d), we normalize the conductances by their respective values at $U_R = U_L$. The values of $G_{\alpha\alpha}(U_R = U_L)$ are shown in table I of the SM [14] and are within the reach of standard state-of-the-art experimental techniques [34].

G_{LL} and G_{RR} as probes for topological phases.— The dependence of G_{LL} and G_{RR} on U_R can be used to distinguish between trivial and topological phases. In Figs. 1 (b) and (c), respectively, we compare G_{LL} and G_{RR} as functions of U_R/U_L for the trivial (dashed lines) and topological (solid lines) regimes for the pristine wire, in the presence of a smooth confining potential, and moderate disorder (with $W = 3.5\Delta$ and averaging over 100 disorder realizations) [35]. Notice that *only in the topological phase* G_{RR} exhibits the same dependence on U_R/U_L as G_{LL} . Strikingly, this result remains true in the presence of inhomogeneities in the wire (green and orange solid lines), with $G_{LL} = G_{RR}$ qualitatively reproducing the nonlocal behavior of the clean case, which signals the robustness of the topological phase. In the trivial phase, quasi-Majoranas and disorder-driven states do not reproduce such a feature, as we can see the stark difference between G_{LL} and G_{RR} (dashed lines). These results also hold for a symmetric profile of the confining potential.

Identifying fine-tuned trivial peaks.— The nonlocality of LAR is an experimentally accessible test of whether left and right zero-bias peaks are correlated. A coincidental appearance of zero-bias peaks at similar regions in parameter space is insufficient as a signature of MZMs. To illustrate this point, we show in Figs. 2 (c) and (d) that fine-tuned *nontopological* ABSs (pink dotted curves) yield $G_{LL} \neq G_{RR}$ as functions of U_R/U_L , consistent with the results for the trivial phase. These nontopological ABSs are symmetrically localized in the normal parts of the wire [1 (a)], which act as quantum wells, and perfectly mimic the zero-bias peak characteristic of MZMs, i.e., $G_{LL} = G_{RR} = 1.99e^2/h$ at $U_R = U_L$ [36]. Upon varying U_R/U_L , one can tell apart these accidental ABSs ($G_{LL} \neq G_{RR}$) from true topological states ($G_{LL} = G_{RR}$). We point out that for significantly smaller wires ($L_S < \xi$), such that the trivial ABSs hybridize, the pink curves could, in principle, mimic the topological case. However, since these ABSs are fine-tuned, the conductance is not robust against variations of the parameters, e.g., μ_N and V_z . For wires of length 2 μm or longer, currently used in experiments [9], our proposal for distinguishing topological from trivial phases by measuring only G_{LL} and G_{RR} works.

Protocol using only G_{LL} & G_{RR} measurements.— Our simplified protocol to distinguish trivial and topological phases in the setup of Fig. 1 (a) can be summarized as follows: (1) for a given set of system parameters, measure the zero-bias local conductance peaks G_{LL}

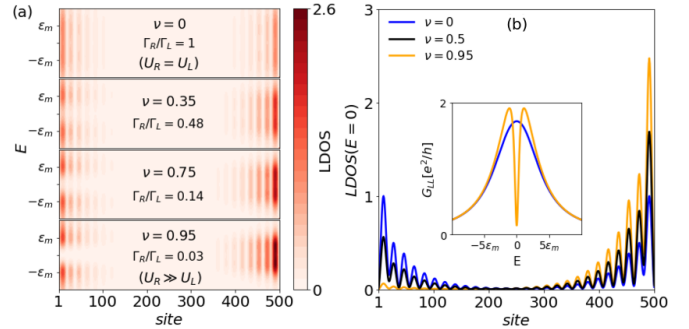


FIG. 3. (a) LDOS (color map) as a function of E for different values of ν . Around zero energy, a dip emerges in the LDOS on the left side due to a stronger coupling to the lead. On the right side, the LDOS is enhanced at zero energy as ν increases ($\Gamma_R \rightarrow 0$). (b) LDOS at $E = 0$ for different values of ν . The LDOS shifts from left to right as the coupling to the right lead decreases, followed by the emergence of a dip in the local conductance (inset). The nanowire parameters are the same as those used in Fig. 2, $V_z = 1.40V_c$, and $\Gamma_L = 1.6\Delta$. We consider ε_m as the energy of the lowest mode. The values of the LDOS were normalized by their maximum at $\nu = 0$.

and G_{RR} as functions of the gate-tunable ratio U_R/U_L (U_L is kept fixed), (2) compare the obtained curves for G_{LL} and G_{RR} : if $G_{LL} \neq G_{RR}$, the system is trivial; if $G_{LL} = G_{RR}$, (3) vary the system parameters within some range [9] and repeat (1) and (2): if the G_{LL} curves remain equal to those for G_{RR} within the entire range of parameters varied, the zero-bias peaks in $G_{LL} = G_{RR}$ vs. U_R/U_L are robust and the system is topological.

Recent works [8, 10, 37] have proposed that a combination of local and nonlocal conductances is required to characterize the topological quantum phase transition. Nonlocal conductance, in general, presents much weaker signals and is more susceptible to noise than the local conductance [9, 12]. As the ratio L_S/ξ increases, the visibility of the topological phase transition in the nonlocal conductance is suppressed [10], limiting the maximum length of the wire [9]. Since the topological protection exponentially increases with L_S , $\varepsilon_m \propto \exp(-L_S/\xi)$ [30], this is an unwanted constraint. Our proposal avoids these issues altogether as it relies only on the local conductance measurements, being particularly suited for long wires.

Local density of states.— The suppression of the (quasi-) zero-energy mediated LAR observed in the topological phase of Fig. 2 (b) can be explained by the emergence of a zero-energy dip in the LDOS at the left side of the wire as Γ_R decreases (i.e., U_R increases), Fig. 3 (a). We obtain the LDOS from the imaginary part of the retarded Green function [38] within the Bogoliubov-de Gennes formalism [39], $\mathcal{G}^r = (E - H_{BdG} - \Sigma)^{-1}$, where Σ is the self-energy.

In Fig. 3 (a) we show the LDOS (color map) as a function of the energy E for $V_z = 1.40V_c$. We observe a suppression around $E = 0$ on the left side of the wire for large

values of the lead-asymmetry $\nu = (\Gamma_L - \Gamma_R)/(\Gamma_L + \Gamma_R)$. More specifically, we show in Fig. 3 (b) the LDOS at $E = 0$ for several values of ν . At $\nu = 0$ ($U_R = U_L \Leftrightarrow \Gamma_R = \Gamma_L$, blue curve), the LDOS has equal weights on the left and right ends of the wire. As Γ_R decreases (i.e., U_R increases) for a fixed Γ_L (U_L), black and orange curves, an asymmetry develops between the left and right sides with the LDOS building up on the right side. The local conductance G_{LL} , which we calculate here analytically for the effective model [14, 28], shows a suppression as Γ_R is decreased [see inset in 3 (b)]. This suppression is similar to those in Figs. 1 (b), (c) and 2(c), (d) as U_R/U_L was increased. In the topological phase, the local conductances are correlated, i.e., $G_{LL} = G_{RR}$, but suppressed for different reasons. While G_{LL} is suppressed due to the emergence of a dip in the LDOS on the left end of the wire, G_{RR} is reduced because the right tunnel barrier U_R increases (i.e., Γ_R is decreased). Therefore, the lead-asymmetry, controlled by the tunnel voltages U_L and U_R , allows us to manipulate the LDOS [40].

A complementary analysis using non-Hermitian topology [41] is provided in the Supplementary Material [14]. Here, the asymmetry in the LDOS can be understood by a bifurcation of the imaginary part of the energy of the lowest mode and its particle-hole partner. This means that one of the Majorana components leaks to the lead, causing the zero-energy dip in the LDOS, while the other has its lifetime increased. It is worth mentioning that after the bifurcation (exceptional point), the real part of the energy of the lowest mode is exactly zero, suggesting that it is possible to artificially create non-hybridized MZMs in finite wires by exploring the lead-asymmetry [41]. However, the suppression of G_{RR} due to the barrier height shows that this is not a true zero-energy Majorana mode, which instead would present a universal zero-bias peak of $2e^2/h$ [42].

Majorana-based transistor.— The manipulation of the LDOS by exploiting the lead-asymmetry as above, allows us to gate-control currents in multi-terminal devices. To illustrate this, we propose a Majorana-based transistor using a QD coupled to leads 1 and 2, and to a Majorana wire [43, 44], Fig. 4 (a). The right side of the topological wire is then coupled to a third lead that acts as a “base-gate” (U_R), controlling the current flow through the QD.

We use an effective model to describe the Majorana wire [45] and show that if the right lead (base-gate) is turned off [$\Gamma_R = 0$, blue curve in Fig. 4 (b)], the conductance is not mediated by the MZM, as the lead-asymmetry enforces a zero-energy dip in the LDOS on the left side of the wire [46]. Since in this situation the Majorana on the right end is uncoupled from the right lead, this characterizes the situation of maximum asymmetry, $\nu = 1$. In agreement with our previous analysis, the QD DOS, ρ_{dot} , and consequently the conductance are negligible, with no contribution from the Majorana mode. The right lead ($\Gamma_R \neq 0$) unlocks the leakage of the

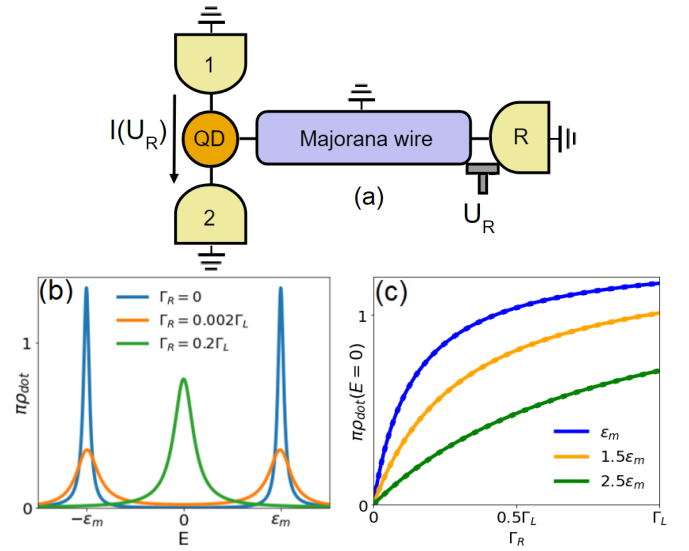


FIG. 4. (a) Setup of the Majorana-transistor: QD coupled to leads 1 and 2 and to a Majorana wire connected to a third lead R . (b) DOS of the QD for different values of Γ_R . The control over the coupling to the right lead (U_R) allows us to manipulate the QD DOS, thus suppressing or enhancing it around zero energy. (c) DOS of the QD at $E = 0$ as a function of Γ_R for different ϵ_m . At $\Gamma_R = 0$, the zero-bias peak vanishes. The parameters used are $t_0 = \Gamma_L = 100\epsilon_m$, and $\epsilon_d = 53.3t_0$.

Majorana mode into the QD [orange and green curves in Fig. 4 (b)]. For large Γ_R , we observe a peak of $e^2/2h$ in the transversal conductance [47]. In Fig. 4 (c), we show how ρ_{dot} evolves as we vary Γ_R and ϵ_m (i.e., the wire length). Note that the longer the wire (blue curve), the sooner the MZM leaks into the QD.

Validity of the proposed protocol.— We have deliberately introduced some possible detrimental effects in our setup, such as (i) nontopological superconducting nanowire segments of length ℓ , (ii) normal ($\Delta = 0$) nanowire sections of length ℓ_N , (iii) potential barriers of different lengths, and/or (iv) strong Anderson disorder [35] [(i), (ii), and (iii) emulate additional nonuniformities; see SM for details of (i), (ii), (iii), and (iv)]. We have verified that our protocol holds provided that $\ell, \ell_N \lesssim 0.6L_S$ and $\sigma/\bar{\mu} \lesssim 3$, with σ the standard deviation and $\bar{\mu}$ the average chemical potential [48]. We emphasize that this is not an exhaustive list of undesirable effects possibly encountered in experimental systems. Within the scope of known sources of trivial modes mimicking MZMs, we have not found any false positives.

Summary.— We theoretically investigated quantum transport in realistic topological wires [9]. We identified the local conductances G_{LL} and G_{RR} as unique probes for topological phases. Our proposed protocol is: (1) measure the zero-bias peaks of G_{LL} and G_{RR} as functions of the asymmetry of the left and right tunnel barriers (U_R/U_L) and (2) compare the curves: if $G_{LL} \neq G_{RR}$ the

zero mode is trivial, else (i.e., if $G_{LL} = G_{RR}$), (3) vary the system parameters and perform (1) and (2) again. If $G_{LL} = G_{RR}$ holds for the entire range of varied parameters, the zero-bias peak is robust and signals a topological phase. In addition, we showed that the LDOS can be controlled via asymmetric couplings to normal leads, and proposed a Majorana-based transistor.

Acknowledgments.— The authors acknowledge valuable discussions with Daniel Loss, Jelena Klinovaja, Henry F. Legg, Richard Hess, and Lucas Pupim. This work was supported by the São Paulo Research Foundation (FAPESP) Grants No. 2016/08468-0 and No. 2020/00841-9, and from Conselho Nacional de Pesquisas (CNPq), Grant No. 306122/2018-9. We also acknowledge support from the Swiss NSF.

[1] A. Y. Kitaev, *Physics-Uspekhi* **44**, 131 (2001).

[2] R. M. Lutchyn, J. D. Sau, and S. Das Sarma, *Phys. Rev. Lett.* **105**, 077001 (2010).

[3] Y. Oreg, G. Refael, and F. von Oppen, *Phys. Rev. Lett.* **105**, 177002 (2010).

[4] V. Mourik, K. Zuo, S. M. Frolov, S. Plissard, E. P. Bakkers, and L. P. Kouwenhoven, *Science* **336**, 1003 (2012).

[5] A. Das, Y. Ronen, Y. Most, Y. Oreg, M. Heiblum, and H. Shtrikman, *Nat. Phys.* **8**, 887 (2012).

[6] M. T. Deng, C. L. Yu, G. Y. Huang, M. Larsson, P. Caroff, and H. Q. Xu, *Nano Lett.* **12**, 6414 (2012).

[7] M. Franz, *Nat. Nanotechnol.* **8**, 149 (2013).

[8] D. I. Pikulin, B. van Heck, T. Karzig, E. A. Martinez, B. Nijholt, T. Laeven, G. W. Winkler, J. D. Watson, S. Heedt, M. Temurhan, V. Svidenko, R. M. Lutchyn, M. Thomas, G. de Lange, L. Casparis, and C. Nayak, *arXiv:2103.12217* (2021).

[9] M. Aghaee and *et al.*, *arXiv:2207.02472* (2022).

[10] T. Rosdahl, A. Vuik, M. Kjaergaard, and A. Akhmerov, *Phys. Rev. B* **97**, 045421 (2018).

[11] R. Hess, H. F. Legg, D. Loss, and J. Klinovaja, *arXiv:2210.03507* (2022).

[12] R. Hess, H. F. Legg, D. Loss, and J. Klinovaja, *Phys. Rev. B* **104**, 075405 (2021).

[13] D. Sahu, V. Khade, and S. Gangadharaiah, *arXiv:2211.03045* (2022).

[14] See supplementary material at:.

[15] J. J. He, T. K. Ng, P. A. Lee, and K. T. Law, *Phys. Rev. Lett.* **112**, 037001 (2014).

[16] F. Setiawan, P. Brydon, J. D. Sau, and S. D. Sarma, *Phys. Rev. B* **91**, 214513 (2015).

[17] B. M. Fregoso, A. M. Lobos, and S. D. Sarma, *Phys. Rev. B* **88**, 180507 (2013).

[18] A. M. Lobos and S. D. Sarma, *New J. Phys.* **17**, 065010 (2015).

[19] C. Reeg and D. L. Maslov, *Phys. Rev. B* **95**, 205439 (2017).

[20] O. A. Awoga, J. Cayao, and A. M. Black-Schaffer, *Phys. Rev. B* **105**, 144509 (2022).

[21] C. Reeg, D. Loss, and J. Klinovaja, *Phys. Rev. B* **97**, 165425 (2018).

[22] A. Vuik, B. Nijholt, A. Akhmerov, and M. Wimmer, *SciPost Physics* **7**, 061 (2019).

[23] T. D. Stanescu and S. Tewari, *Phys. Rev. B* **100**, 155429 (2019).

[24] C. W. Groth, M. Wimmer, A. R. Akhmerov, and X. Waintal, *New J. Phys.* **16**, 063065 (2014).

[25] A low-energy effective model [28, 49] describing the coupling between Majoranas is represented by $H = i\varepsilon_m \gamma_1 \gamma_2$, where γ_i is the Majorana operator. In this case, the topological ABSs eigenenergies are $\pm\varepsilon_m$.

[26] G. Wang, T. Dvir, G. P. Mazur, C.-X. Liu, N. van Loo, S. L. D. ten Haaf, A. Bordin, S. Gazibegovic, G. Badawy, E. P. A. M. Bakkers, M. Wimmer, and L. P. Kouwenhoven, *Nature* **612**, 448 (2022).

[27] In an NSN junction, $A_{\uparrow\uparrow}^R \approx 1 - \Delta^2/2V_z^2$, $A_{\downarrow\downarrow}^R \approx \Delta^4/16V_z^4$, $A_{\uparrow\downarrow}^R = A_{\downarrow\uparrow}^R \approx \Delta^2/4V_z^2$, such that $A_R \approx 1$. Note that as V_z increases, the dominant component is $A_{\uparrow\uparrow}^R$. Here the MZM on the right side of the wire couples more strongly to the spin-up component of the incident electron, as opposed to the MZM on the left side, which couples more strongly to the spin down [14]. In this approximate description of the pristine wire, we verify that $A_L = A_R$.

[28] J. Nilsson, A. Akhmerov, and C. Beenakker, *Phys. Rev. Lett.* **101**, 120403 (2008).

[29] E. Prada, P. San-Jose, and R. Aguado, *Phys. Rev. B* **86**, 180503 (2012).

[30] S. D. Sarma, J. D. Sau, and T. D. Stanescu, *Phys. Rev. B* **86**, 220506 (2012).

[31] D. Rainis, L. Trifunovic, J. Klinovaja, and D. Loss, *Phys. Rev. B* **87**, 024515 (2013).

[32] G. Blonder, M. M. Tinkham, and K. T. Klapwijk, *Phys. Rev. B* **25**, 4515 (1982).

[33] J. Klinovaja and D. Loss, *Phys. Rev. B* **86**, 085408 (2012).

[34] J.-Y. Wang, N. van Loo, G. P. Mazur, V. Levajac, F. K. Malinowski, M. Lemang, F. Borsoi, G. Badawy, S. Gazibegovic, E. P. A. M. Bakkers, M. Quintero-Pérez, S. Heedt, and L. P. Kouwenhoven, *Phys. Rev. B* **106**, 075306 (2022).

[35] H. Pan and S. D. Sarma, *Phys. Rev. B* **103**, 224505 (2021).

[36] The nontopological ABSs here are engineered following Ref. [12]. We set the spin-orbit coupling α_R to zero within the superconducting region of the nanowire and choose $V_z = 1.16V_c$ and $\mu_N = 2.58meV$.

[37] H. Pan, J. D. Sau, and S. D. Sarma, *Phys. Rev. B* **103**, 014513 (2021).

[38] S. Datta, *Electronic transport in mesoscopic systems* (Cambridge university press, 1997).

[39] In agreement with the LDOS obtained using the package KWANT [24].

[40] Our analysis is smoothly connected to the results of Ref. [50], in which the author shows that if the system has only one lead (i.e., $\Gamma_R = 0 \Leftrightarrow \nu = 1$), the conductance vanishes for an even number of MZMs.

[41] J. Avila, F. Peñaranda, E. Prada, P. San-Jose, and R. Aguado, *Communications Physics* **2**, 1 (2019).

[42] K. T. Law, P. A. Lee, and T. K. Ng, *Phys. Rev. Lett.* **103**, 237001 (2009).

[43] D. E. Liu and H. U. Baranger, *Phys. Rev. B* **84**, 201308 (2011).

[44] E. Vernek, P. Penteado, A. Seridonio, and J. Egues, *Phys. Rev. B* **89**, 165314 (2014).

- [45] M. Leijnse and K. Flensberg, *Phys. Rev. B* **84**, 140501 (2011).
- [46] Due to interference the LDOS is strictly zero only at $E = 0$.
- [47] R. A. Dourado, P. H. Penteado, and J. C. Egues, to be submitted (2022).
- [48] We note that, even in the moderate disorder case, there may be rare disorder realizations having correlated zero-bias peaks (due to hybridization of the trivial modes); these are irrelevant if self averaging holds, otherwise, these zero-energy modes fall under ‘fine-tuned’ cases.
- [49] C. Nayak, S. H. Simon, A. Stern, M. Freedman, and S. D. Sarma, *Rev. Mod. Phys.* **80**, 1083 (2008).
- [50] K. Flensberg, *Phys. Rev. B* **82**, 180516 (2010).

Supplemental Material for “Nonlocality of local Andreev conductances as a probe for topological Majorana wires”

Rodrigo A. Dourado,¹ Poliana H. Penteado,¹ and J. Carlos Egues^{1,2}

¹*Instituto de Física de São Carlos, Universidade de São Paulo, 13560-970 São Carlos, São Paulo, Brazil*

²*Department of Physics, University of Basel, Klingelbergstrasse 82, CH-4056 Basel, Switzerland*

SEMICONDUCING NANOWIRE: CONDUCTANCE SIMULATIONS

For the numerical calculation, we discretize the continuum BdG Hamiltonian in Eq. (1) of the main text and obtain the tight binding model [1]

$$H_{\text{TB}} = \sum_{j=1}^{N-1} [-t|j+1\rangle\langle j|\tau_z + i\alpha|j+1\rangle\langle j|\sigma_y\tau_z + \text{H.c.}] + \sum_{j=1}^N [\Delta|j\rangle\langle j|\tau_x + (2t - \mu_j)|j\rangle\langle j|\tau_z + V_z|j\rangle\langle j|\sigma_x] \quad (\text{S1})$$

where $t = \hbar^2/2m^*a^2$ and $\alpha = \alpha_R/2a$, with $a = 5 \text{ nm}$ [2].

For clarity, the conductances G_{LL} and G_{RR} in Figs. 1 (b), (c), and 2 (c), (d) were normalized by their respective values at $U_R = U_L$, G_{LL}^{sym} and G_{RR}^{sym} . In Table I, we show the values of G_{LL}^{sym} and G_{RR}^{sym} for the pristine wire and in the presence of a smooth confining potential at $V_z/V_c = 0.10, 0.95, 1.15$, and 1.40 . For the pristine wire, we also show the case $V_z/V_c = 1.20$ and the fine-tuned ABS in a nontopological nanowire (no spin-orbit coupling in the superconducting part of the wire) [2] .

Pristine wire		
V_z/V_c	$G_{LL}(U_R = U_L)[e^2/h]$	$G_{RR}(U_R = U_L)[e^2/h]$
0.10	0.012	0.012
0.95	0.038	0.038
1.15	1.997	1.997
1.20	1.999	1.999
1.40	1.995	1.995
NT – ABS	1.991	1.991

Smooth confining potential		
V_z/V_c	$G_{LL}(U_R = U_L)[e^2/h]$	$G_{RR}(U_R = U_L)[e^2/h]$
0.10	0.015	0.012
0.95	0.178	0.044
1.15	1.997	1.997
1.40	1.927	1.927

TABLE I. Local conductances G_{LL} and G_{RR} at $U_L = U_R$ for the pristine wire and in the presence of a smooth confining potential. The parameters are detailed in Fig. 1 of the main text.

In Fig. S1 (a), we show the spectrum of the pristine nanowire [superconducting section of the wire in Fig. 1 (a)] as a function of V_z/V_c . The bulk topological phase transition occurs at $V_c = \sqrt{\Delta^2 + \mu^2}$ (vertical red line). For $V_z > V_c$, the Majorana zero modes located at the ends of the wire mediate a zero-bias conductance peak [Figs. 1 (b), (c) and 2 (c), (d) of the main text], which is dominated by LAR processes, as shown in Fig S1 (b). As we shall discuss in the next section, the direct tunneling (T_{RL} , blue line) and crossed Andreev reflection (A_{RL} , orange line) have the same amplitude and increase with the hybridization energy between the MZMs located at opposite ends of the wire. We observe that as the energy of the lowest mode (topological ABS) reach a local maximum due to the oscillations seen in Fig. S1 (a) [3–5], T_{RL} and A_{RL} also peak. These numerical results are consistent with the findings obtained via an effective model describing only the lowest modes coupled to metallic leads [6], as we show in the following.

LOW-ENERGY EFFECTIVE HAMILTONIAN

In this section, we derive a low-energy effective Hamiltonian for the nanowire and its coupling to metallic leads. We start with a simple normal/superconductor (NS) junction with the superconductor in the topological phase.

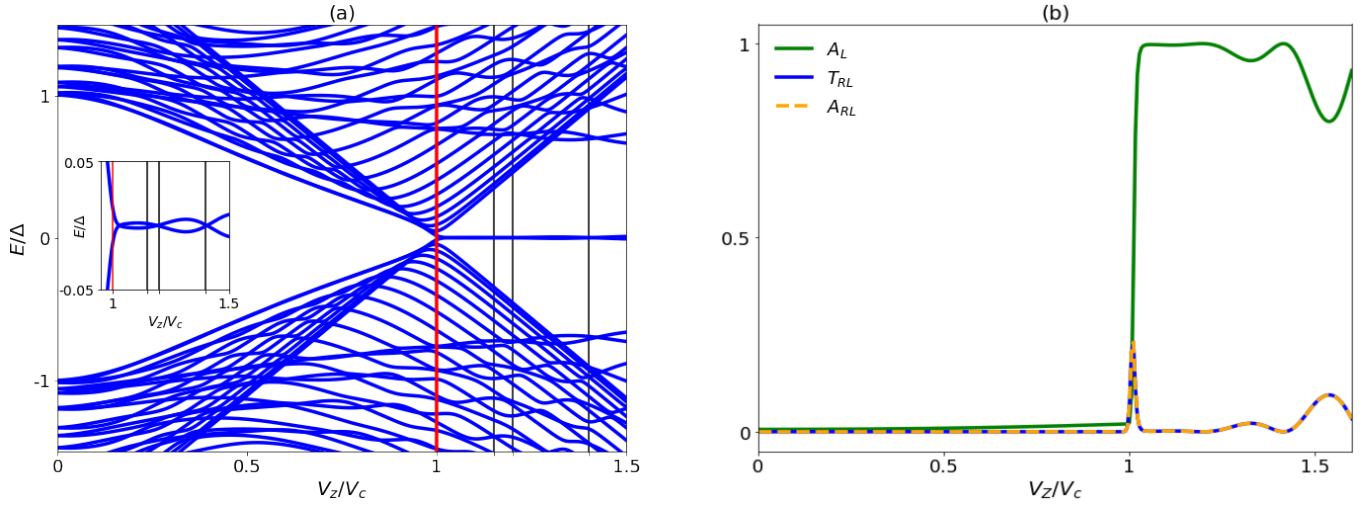


FIG. S1. (a) Spectra of the pristine superconducting nanowire, described by equation (S1) as a function of the Zeeman field. In the inset, we show the Majorana oscillations. (b) Transmission probabilities for local Andreev reflection (blue), $A_L = A_R$, direct transport (green), $T_{RL} = T_{LR}$, and crossed Andreev reflection (orange), $A_{RL} = A_{LR}$, as a function of the Zeeman field. We note by comparing (a) and (b) that T_{RL} and A_{RL} follow the oscillations of the energy of the lowest mode. In addition, the conductance is dominated by LAR, which is enhanced by the emergence of the MZMs, in the regime of parameters considered. The parameters for the nanowire are detailed in Fig 2.

Projection onto the N + S basis, described by the eigenvectors $|N\rangle$ and $|S\rangle$, results in the tunneling Hamiltonian

$$H_T = \sum_{\sigma=\uparrow,\downarrow} t_\sigma c_\sigma^\dagger(0) \psi_\sigma(0) + t_\sigma^* \psi_\sigma^\dagger(0) c_\sigma(0), \quad (\text{S2})$$

where $t_\sigma = \langle N | H | S \rangle$, with H the total Hamiltonian of the uncoupled system. Here, we use $c_\sigma(x) = \int dk c_{k,\sigma} e^{ikx}$ and $\psi_\sigma(x)$ to denote the annihilation operators on the normal and superconducting segments of the wire, respectively. Since the superconductor is in the topological phase, there is a Majorana mode localized near the domain wall at $x = 0$, whose operator is $\gamma = \int dx [f\psi_\uparrow(x) + g\psi_\downarrow(x) + f^*\psi_\uparrow^\dagger(x) + g^*\psi_\downarrow^\dagger(x)]$ [7]. The spinor $\varphi^\dagger = (f \ g \ g^* \ -f^*)$ defining such an operator is obtained by solving the equation $\mathcal{H}\varphi(x) = 0$, where \mathcal{H} is the Bogoliubov-de Gennes Hamiltonian of the superconducting nanowire in the basis $\{\psi_\uparrow(x), \psi_\downarrow(x), \psi_\uparrow^\dagger(x), -\psi_\downarrow^\dagger(x)\}$. Additionally, we expand the operators $\psi_\sigma(x)$ in the basis of the excitations of the superconductor $\psi_{\uparrow(\downarrow)}(x) = f(g)\gamma + \dots$ [8]. We then make the assumption $\psi_{\uparrow(\downarrow)} \sim f(g)\gamma$, with $|f|^2 + |g|^2 = 1$ [9], which is a good approximation in the low-bias limit, where the main contribution to the conductance comes from the MZM. Using these operators in Eq. (S2) we obtain

$$H_T = t\gamma \left[f c_\uparrow(0) + g c_\downarrow(0) - f^* c_\uparrow^\dagger(0) - g^* c_\downarrow^\dagger(0) \right], \quad (\text{S3})$$

with $t_\uparrow = t_\downarrow = t$ (unpolarized metal) real.

It is possible to further simplify the Hamiltonian above if one performs a unitary transformation such that $\Psi_1 = f c_\uparrow + g c_\downarrow$ and $\Psi_2 = -g^* c_\uparrow + f^* c_\downarrow$, which yields

$$H_T = t\gamma \left[\Psi_1(0) - \Psi_1^\dagger(0) \right], \quad (\text{S4})$$

i.e., the Majorana only couples to one type of electron in the metal [9].

Local Andreev Reflection Coefficients

Here we explicitly show that the spin-dependent local Andreev reflection coefficients shown in Fig. 2 (a) of the main text can be traced back to the Majorana wavefunction. We use the scattering matrix formalism [6, 10] and calculate the S-matrix for an NS junction,

$$S(E) = 1 - 2\pi i\rho W^\dagger (E - \mathcal{H} + i\pi\rho W W^\dagger)^{-1} W, \quad (\text{S5})$$

where \mathcal{H} is the BdG Hamiltonian of the nanowire, which is zero for a semi-infinite wire in the low-energy regime, ρ is the density of states of the normal lead, and $W = t(f \ g \ -f^* \ -g^*)$ in the basis $\{\Phi_{e,\uparrow}, \Phi_{e,\downarrow}, \Phi_{h,\uparrow}, \Phi_{h,\downarrow}\}$ of propagating electrons and holes in the lead. By substituting W into Eq. (S5) we obtain

$$S(E) = \begin{pmatrix} R^{ee} & A^{eh} \\ A^{he} & R^{hh} \end{pmatrix} = 1 - \frac{i\Gamma}{E + i\Gamma} \begin{pmatrix} |f|^2 & f^*g & -(f^*)^2 & -f^*g^* \\ g^*f & |g|^2 & -g^*f^* & -(g^*)^2 \\ -f^2 & -fg & |f|^2 & g^*f \\ -fg & -g^2 & f^*g & |g|^2 \end{pmatrix}, \quad (\text{S6})$$

with $\Gamma = 2\pi\rho t^2$, $R^{ee(hh)}$ and $A^{he(eh)}$ the normal and Andreev reflection matrices, respectively. In particular, A^{he} at $E = 0$ is given by

$$A^{he} = \begin{pmatrix} a_{\uparrow\uparrow} & a_{\uparrow\downarrow} \\ a_{\downarrow\uparrow} & a_{\downarrow\downarrow} \end{pmatrix} = \begin{pmatrix} f^2 & fg \\ fg & g^2 \end{pmatrix}. \quad (\text{S7})$$

Therefore, the Andreev components $A_{\sigma\sigma'}^L = |a_{\sigma\sigma'}|^2$ gives us approximately the polarization of the Majorana bound state. As we increase the Zeeman field [Fig. 2 (a) of the main text], the Majorana wavefunction starts to polarize in the spin-down direction. Hence as $|g|^2$ increases and $|f|^2$ decreases, $A_{\downarrow\downarrow}^L$ becomes the dominant process, which is already visible at $V_z/V_c \approx 1.40$. The transition between the spinfull (small V_z) and the Kitaev chain (large V_z) regimes can be observed by measuring the individual Andreev reflection components.

One of the signatures of a MZM is a quantized conductance of $2e^2/h$, even in the presence of two spin channels in the leads. This is distinct from the conductance for the BTK model [11], which can reach $4e^2/h$. As shown in Eq. (S4), this is because the Majorana only couples to electrons with a certain spin polarization; from Eq. (S6) we obtain that $R_L = \sum_{\sigma\sigma'} |r_{\sigma\sigma'}|^2 = A_L = \sum_{\sigma\sigma'} |a_{\sigma\sigma'}|^2 = 1$, with $r_{\sigma\sigma'}$ the coefficients of matrix R^{ee} . This result can be understood by rewriting the S-matrix equation, relating incoming and outgoing electrons/holes, using the transformed basis $\{\psi_1, \psi_2, \psi_1^\dagger, \psi_2^\dagger\}$, i.e.,

$$U^\dagger \Phi^{(\text{out})}(E) = U^\dagger S(E) U U^\dagger \Phi^{(\text{in})}(E), \quad (\text{S8})$$

with $\Phi^{(\text{in/out})}(E) = (\Phi_{e,\uparrow} \ \Phi_{e,\downarrow} \ \Phi_{h,\uparrow} \ \Phi_{h,\downarrow})^T$ and

$$U^\dagger = \begin{pmatrix} \mathcal{U} & 0 \\ 0 & \mathcal{U}^* \end{pmatrix}, \quad \mathcal{U} = \begin{pmatrix} f & g \\ -g^* & f^* \end{pmatrix}. \quad (\text{S9})$$

The S-matrix equation then becomes

$$\begin{pmatrix} \psi_1(E) \\ \psi_2(E) \\ \psi_1^\dagger(E) \\ \psi_2^\dagger(E) \end{pmatrix}^{(\text{out})} = \begin{pmatrix} \frac{E}{E+i\Gamma} & 0 & \frac{i\Gamma}{E+i\Gamma} & 0 \\ 0 & 1 & 0 & 0 \\ \frac{i\Gamma}{E+i\Gamma} & 0 & \frac{E}{E+i\Gamma} & 0 \\ 0 & 0 & 0 & 1 \end{pmatrix} \begin{pmatrix} \psi_1(E) \\ \psi_2(E) \\ \psi_1^\dagger(E) \\ \psi_2^\dagger(E) \end{pmatrix}^{(\text{in})}. \quad (\text{S10})$$

As previously mentioned, there is no coupling between the subspaces of electrons 1 and 2, which ensures that all reflections are “spin-conserving”. Moreover, incident type-2 electrons (holes) are always reflected as electrons (holes) with the same spin polarization, which means that this mode is effectively decoupled from the problem. Hence, the low-energy Hamiltonian of a Majorana wire coupled to external leads is spinless even outside of the strong Zeeman field regime. Finally, at $E = 0$ we have perfect Andreev reflection of type-1 electrons and holes. The Andreev reflection matrix in the new basis at $E = 0$ is

$$\tilde{A}^{he} = \begin{pmatrix} a_{11} & a_{12} \\ a_{21} & a_{22} \end{pmatrix} = \begin{pmatrix} 1 & 0 \\ 0 & 0 \end{pmatrix}. \quad (\text{S11})$$

Conductance of a Majorana wire in a three-terminal device

We now show the derivation of the Majorana wire conductance for an NSN junction using the low-energy effective Hamiltonian $H_M = i\varepsilon_m \gamma_1 \gamma_2$, where ε_m is the hybridization energy. As discussed in the previous section, the Majorana

bound state couples to only one spin-channel. This allows us to consider a spinless model for the leads without any loss of generality.

Here we follow the derivation of the S-matrix presented in Ref. [6]. In the basis $(\Phi_{L,e} \ \Phi_{R,e} \ \Phi_{L,h} \ \Phi_{R,h})^T$ of propagating electrons and holes in leads left L and right R , we have

$$S(E) = \begin{pmatrix} 1+A & A \\ A & 1+A \end{pmatrix}, \quad (S12)$$

where

$$A = Z^{-1} \begin{pmatrix} i\Gamma_L(E + i\Gamma_R) & -\varepsilon_m \sqrt{\Gamma_L \Gamma_R} \\ \varepsilon_m \sqrt{\Gamma_L \Gamma_R} & i\Gamma_R(E + i\Gamma_L) \end{pmatrix}, \quad Z = \varepsilon_m^2 - (E + i\Gamma_L)(E + i\Gamma_R), \quad (S13)$$

with $\Gamma_\alpha = 2\pi|t_\alpha|^2$. The matrix A contains the crossed (off-diagonal terms) and local (diagonal) Andreev reflections.

The zero-bias conductance in lead α is obtained via the current expression [10, 11]

$$I_\alpha = \frac{e}{h} \int dE (2A_\alpha + T_{\beta\alpha} + A_{\beta\alpha}) \tilde{f}(\mu_\alpha) - \frac{e}{h} \int dE (T_{\alpha\beta} - A_{\beta\alpha}) \tilde{f}(\mu_\beta), \quad (S14)$$

where A_α , $T_{\beta\alpha}$, and $A_{\beta\alpha}$ are the probabilities of an incoming electron to be reflected as a hole in the same lead α and transmitted as an electron or as a hole to lead β , respectively, obtained from the S-matrix, $\tilde{f}(\mu_\alpha) = f(E - \mu_\alpha) - f(E)$, $f(E) = [1 + e^{(\beta E)}]^{-1}$ is the Fermi function, and μ_α is the chemical potential of lead α with respect to the chemical potential of the superconducting lead. In all conductance calculations we consider $T = 0$ and small bias voltages.

The local conductance in the left lead is given by

$$G_{LL} = \frac{e^2}{h} (2A_L + T_{RL} + A_{RL})|_{E \rightarrow 0} = \frac{2e^2}{h} \frac{\Gamma_L \Gamma_R}{\varepsilon_m^2 + \Gamma_L \Gamma_R} = \frac{2e^2}{h} \frac{\Gamma^2 - \gamma_0^2}{\varepsilon_m^2 + \Gamma^2 - \gamma_0^2}, \quad (S15)$$

where

$$A_L = |A_{11}|^2 = \frac{\Gamma_L^2 \Gamma_R^2}{(\varepsilon_m^2 + \Gamma_L \Gamma_R)^2}, \quad (S16)$$

$$T_{RL} = A_{RL} = |A_{12}|^2 = \frac{\varepsilon_m^2 \Gamma_L \Gamma_R}{(\varepsilon_m^2 + \Gamma_L \Gamma_R)^2}, \quad (S17)$$

with A_{ij} elements of the matrix (S13), $\Gamma = (\Gamma_L + \Gamma_R)/2$ and $\gamma_0 = (\Gamma_L - \Gamma_R)/2$. As the asymmetry grows ($\Gamma, \gamma_0 \rightarrow 1$), the conductance is suppressed, in agreement with Fig. 3 of the main text. In the limit where one of the leads is decoupled ($\Gamma = \gamma_0$), it vanishes [12]. Note here that, the processes T_{RL} and A_{RL} qualitatively describe the behavior shown in Fig. S1 (b) for the full model. Whenever E/Δ crosses zero ($\varepsilon_m \rightarrow 0$) in S1 (a), A_L is enhanced [Fig. S1 (b)]; T_{RL} and A_{RL} , on the other hand, peak when E/Δ has a maximum (ε_m increases), in agreement with Eq. (S17).

VALIDITY OF THE PROPOSED PROTOCOL

In order to assess the credibility and robustness of our protocol and possibly emulate experimental setups, we introduce additional nonuniformities to our superconducting nanowire segment, and vary the disorder strength. We consider four different scenarios: (i) nontopological superconducting nanowire segment of length ℓ , Figs. S2 and S3, (ii) nonsuperconducting nanowire segment of length ℓ_N , Figs. S4, (iii) asymmetric potential barriers, Fig. S5, and (iv) stronger disorder, i.e., $\sigma/\bar{\mu} > 1$ [1], where σ is the variance and $\bar{\mu}$ is the mean value, Fig. S6. We find that, for the regime of parameters considered here (the parameters are detailed in Figs. 1 and 2 of the main text), the protocol is valid as long as $\ell, \ell_N \lesssim 0.6L_S$. For larger values of ℓ and ℓ_N , it is still possible to observe a suppression of G_{LL} as U_R increases, but after an initial dip, the conductance attains a plateau, similarly to the quasi-Majorana case. For (iv), we find that, on average, the same behavior mentioned above for cases (i) and (ii) starts to occur within the range $2.5 \lesssim \sigma/\bar{\mu} \lesssim 3$. For case (iii), we consider the right side barrier with lengths $L_{b,R} = 0.04$ and $0.08 \mu\text{m}$ (for the left barrier $L_{b,L} = 0.02 \mu\text{m}$). We find that the correlation $G_{LL} = G_{RR}$ holds, and the conductance suppression due to the increase of U_R is more pronounced for larger $L_{b,R}$.

(i) Nontopological superconducting nanowire segment

Here we consider another nonuniform profile for μ_S , the chemical potential of the SC section of the nanowire. We choose a segment of length l , either located at one of the ends [Fig. S2 (a) and (d)] or in the middle of the SC nanowire [Fig. S3 (a) and (d)], whose chemical potential $\tilde{\mu} = 2$ is such that this segment is in the trivial regime.

In Figs. S2 (a) and (d), we show $\mu_S(x)$ as a function of x for $\ell = 0.375$ and $1.5 \mu\text{m}$ ($0.6L_S$), respectively. We note that G_{LL} and G_{RR} are still similarly suppressed when $V_z > V_c$, signaling the topological phase. For larger values of ℓ , our protocol breaks down since G_{LL} and G_{RR} are suppressed differently, see some examples below. In this case, we can no longer distinguish between the trivial and nontrivial regimes.

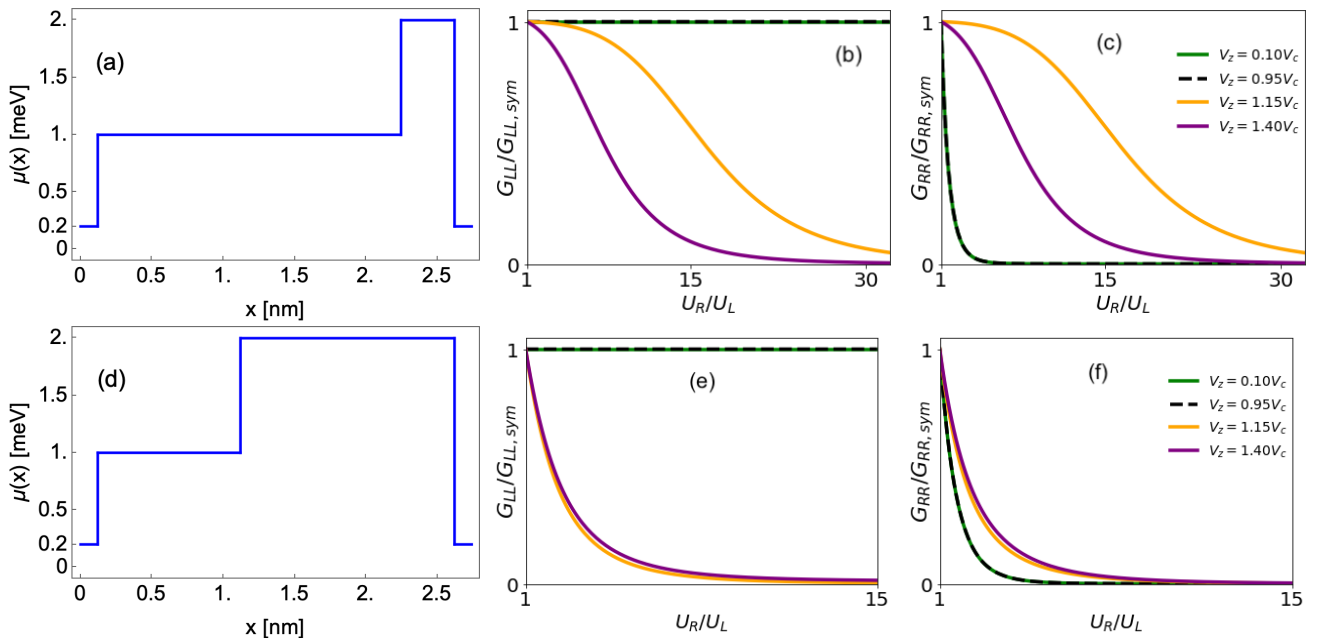


FIG. S2. Chemical potential profile for a trivial region ($\tilde{\mu} = 2$) of length (a) $\ell = 0.375$ nm and (d) $\ell = 1.5$ nm. G_{LL} and G_{RR} as functions of U_R/U_L for (b), (c) the profile in (a), and (e), (f) the profile in (d).

Similarly in Figs. S3 (a) and (d), we show $\mu_S(x)$ for a segment $\ell = 0.5$ and 1.5 nm, respectively, located in the middle of the SC nanowire. The curves for G_{LL} and G_{RR} , especially in (e) and (f), start to differ from each other and our protocol can no longer identify the topological phase.

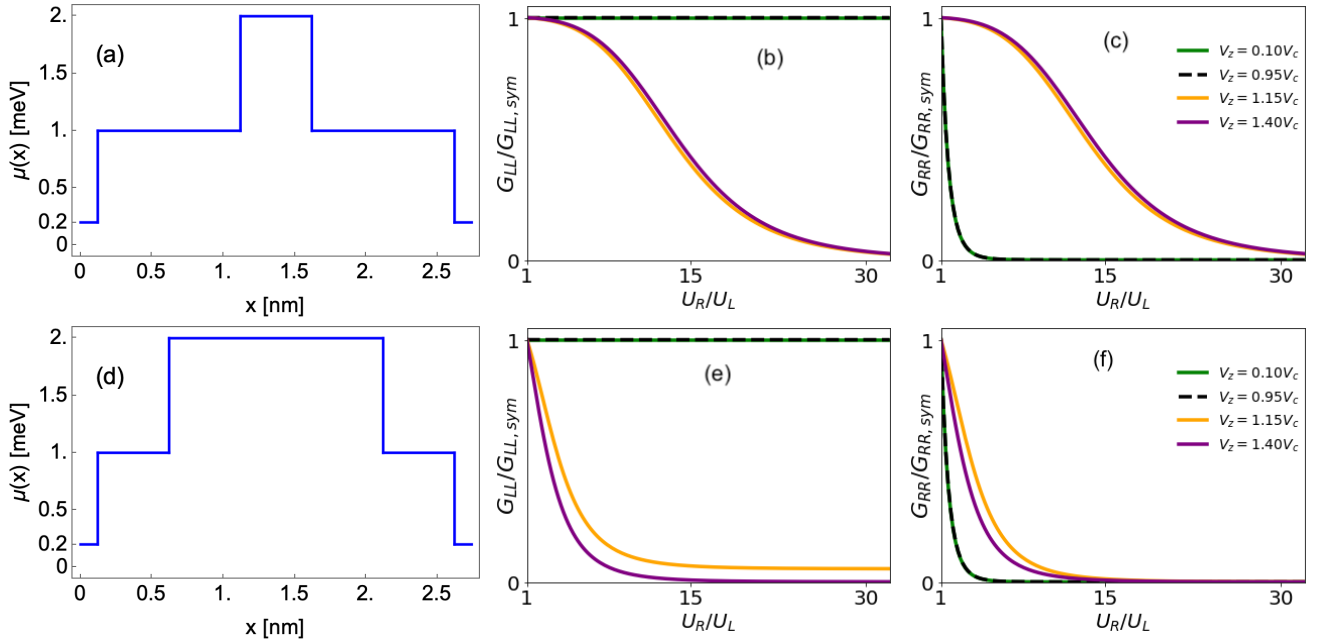


FIG. S3. Chemical potential profile for a trivial region ($\tilde{\mu} = 2$) of length (a) $\ell = 0.5$ nm and (d) $\ell = 1.5$ nm. G_{LL} and G_{RR} as functions of U_R/U_L for (b), (c) the profile in (a), and (e), (f) the profile in (d).

(ii) Nonsuperconducting nanowire segment

Here we modify the profile of the superconducting pairing potential Δ and introduce a segment, ℓ_N , in the middle of the SC nanowire for which $\Delta = 0$.

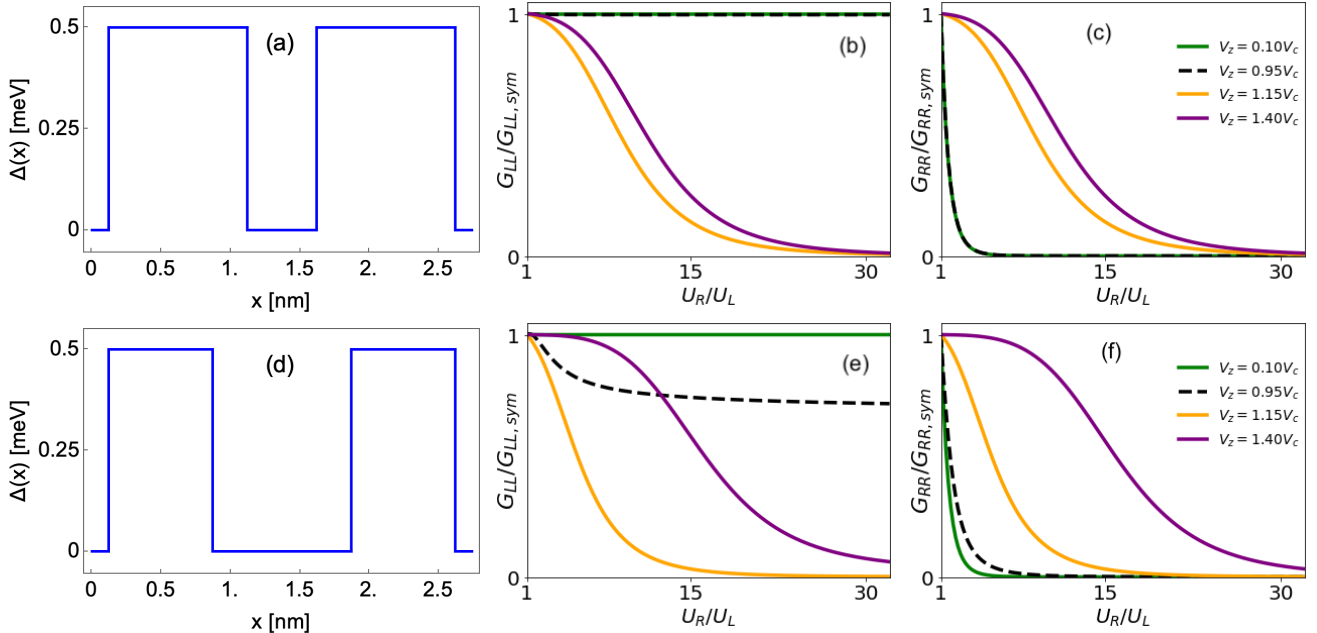


FIG. S4. Superconducting pairing potential profile for a trivial region ($\Delta = 0$) of length (a) $\ell = 0.5$ nm and (d) $\ell = 1.0$ nm. G_{LL} and G_{RR} as functions of U_R/U_L for (b), (c) the profile in (a), and (e), (f) the profile in (d).

(iii) Asymmetric potential barriers

In Fig. S5 (a), we show the potential barrier profile for $L_{b,R} = 4L_{b,L}$. The conductances G_{LL} and G_{RR} , Fig S5 (b) and (c), respectively, still behave similarly. We observe that they are suppressed more rapidly when $L_{b,R}$ increases (not shown).

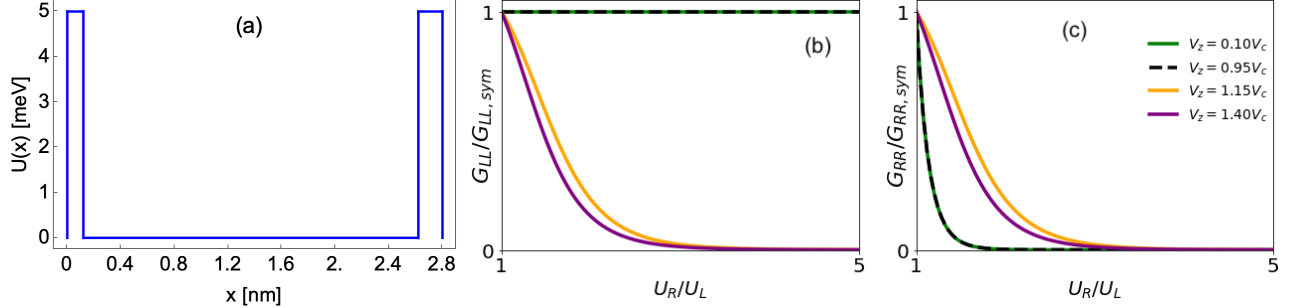


FIG. S5. (a) Potential barrier profile: $L_{b,L} = 0.02$ nm (left) and $L_{b,R} = 0.08$ nm. (b) G_{LL} and (c) G_{RR} as functions of U_R/U_L .

(iv) Stronger disorder

Here we show G_{LL} and G_{RR} as functions of U_R/U_L for two different strengths of disorder: Figs. S6 (a) and (b) $\sigma/\bar{\mu} = 1.5$ and (c) and (d) $\sigma/\bar{\mu} = 3.0$. As previously mentioned, for $\sigma/\bar{\mu} = 3.0$ our protocol is no longer valid, since G_{LL} and G_{RR} are suppressed differently.

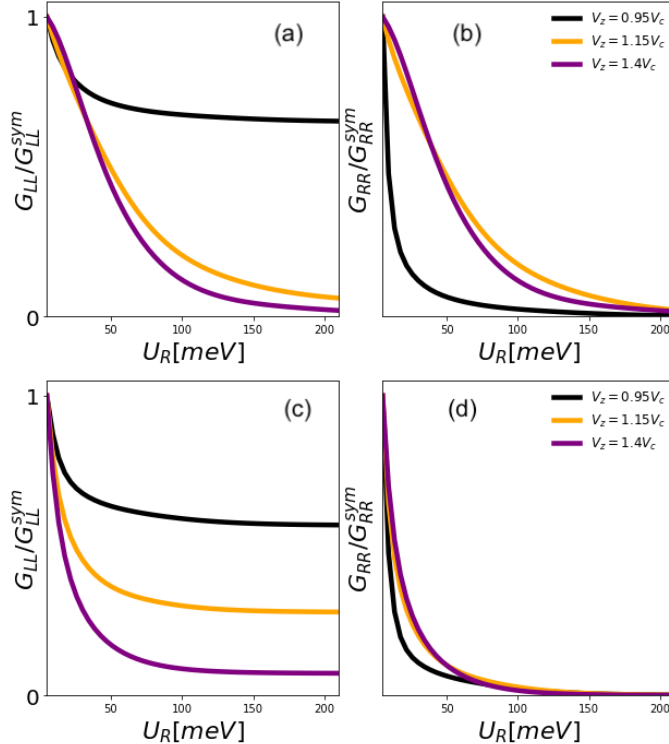


FIG. S6. G_{LL} and G_{RR} as functions of U_R/U_L for (a), (b) $\sigma/\bar{\mu} = 1.5$ and (c), (d) $\sigma/\bar{\mu} = 3.0$.

NON-HERMITIAN TOPOLOGY AND EXCEPTIONAL POINTS

In this section we explore the physics of Exceptional Points (EPs) [13] as a complement to our analysis of the LDOS via Green functions. First, we project the Hamiltonian of the Majorana wire in the low energy subspace H_M using the BdG formalism, and add the self-energy $\Sigma_\alpha = -i\Gamma_\alpha$ to it, similarly to what was done in Ref. [14]. The non-Hermitian Hamiltonian reads

$$H_{\text{eff}} = \frac{1}{2} \begin{pmatrix} \gamma_1 & \gamma_2 \\ -i\Gamma_L & i\varepsilon_m \\ -i\varepsilon_m & -i\Gamma_R \end{pmatrix} \begin{pmatrix} \gamma_1 \\ \gamma_2 \end{pmatrix}. \quad (\text{S18})$$

It is convenient to rewrite the coupling to the leads in terms of symmetric Γ and anti-symmetric γ_0 parts. Note also that the lead-asymmetry defined in the main text is $\nu = \gamma_0/\Gamma$. The BdG Hamiltonian then becomes

$$\mathcal{H}_{\text{eff}} = \begin{pmatrix} -i\Gamma - i\gamma_0 & i\varepsilon_m \\ -i\varepsilon_m & -i\Gamma + i\gamma_0 \end{pmatrix}, \quad (\text{S19})$$

whose eigenenergies and eigenvectors are

$$\varepsilon_\pm = -i\Gamma \pm \sqrt{\varepsilon_m^2 - \gamma_0^2} \quad (\text{S20})$$

and

$$|\phi_\pm\rangle = \begin{pmatrix} 1 \\ a_\pm \end{pmatrix}, \quad a_\pm = \frac{\gamma_0 \pm \sqrt{\gamma_0^2 - \varepsilon_m^2}}{\varepsilon_m}. \quad (\text{S21})$$

The EPs arise when the eigenvectors of the non-Hermitian Hamiltonian coalesce into one, in this case $|\phi_+\rangle = |\phi_-\rangle$, i.e. $a_+ = a_-$. It is easy to see that this occurs when $\gamma_0 = \pm\varepsilon_m$, and therefore there are two EPs. For $\gamma_0^2 > \varepsilon_m^2$, the real part of the eigenenergy goes to zero, while the imaginary part bifurcates into $\Gamma_\pm = -(\Gamma \pm \sqrt{\gamma_0^2 - \varepsilon_m^2})$. This result can be understood as one of the Majorana modes leaking into one of the leads (Γ_+) while the other has an increased lifetime (Γ_-). Interestingly, the leakage does not depend only on the coupling of the Majorana to its respective lead. For example, if we fix Γ_L and *decrease* Γ_R , the left Majorana starts to leak *more* to the left lead as γ_0 increases. This is a consequence of the nonlocality of the Majorana wavefunction. In the main text the same conclusions are obtained by solving the Green functions; for large ν , a gap emerges in the LDOS on the side that is more strongly coupled to the lead, as shown in Fig. 3.

To illustrate the behavior above, we numerically obtain the spectrum of the open system using the full Kitaev chain, described by the Hamiltonian

$$H_K = -\mu \sum_{j=1}^N c_j^\dagger c_j + \sum_{j=1}^{N-1} \left(\Delta c_j^\dagger c_{j+1}^\dagger - t c_j^\dagger c_{j+1} + \text{H.c.} \right), \quad (\text{S22})$$

for $N = 15$, $\mu/\Delta = 2$, $\Gamma_L = 5\varepsilon_m$, $\gamma_0 = 190\varepsilon_m$, and $\nu = 0.95$. The hybridization energy ε_m (energy of the lowest mode), used as a reference here, was obtained at $t/\Delta = 2.5$ for the closed system. In Fig. S7 (a) we show E/Δ as a function of the hopping parameter t/Δ . We note that whenever the energy, which oscillates as t/Δ increases, is smaller than γ_0 , there is a bifurcation in the imaginary part of the eigenenergy while its real part goes to zero. In Fig. S7 (b), we show the probability densities for the two lowest modes for $t/\Delta = 2$, indicated in Fig. S7 (a) by the green and orange points. We note that the imaginary part of the energy of the Majorana on the left (orange) is larger than the one located on the right (green). This means that it leaks faster to the lead, in agreement with the the result (gap in the LDOS) in Fig. 3 of the main text. We point out that if we fix Γ_R and vary Γ_L instead, the behavior of left and right Majoranas invert in terms of the imaginary part of the energy, i.e., the system is symmetric with respect to varying Γ_R (Γ_L) and keeping Γ_L (Γ_R) fixed. In conclusion, if we keep the parameters constant, and therefore ε_m , the emergence of the exceptional points can be controlled by the asymmetry in the coupling to the left and right leads ν .

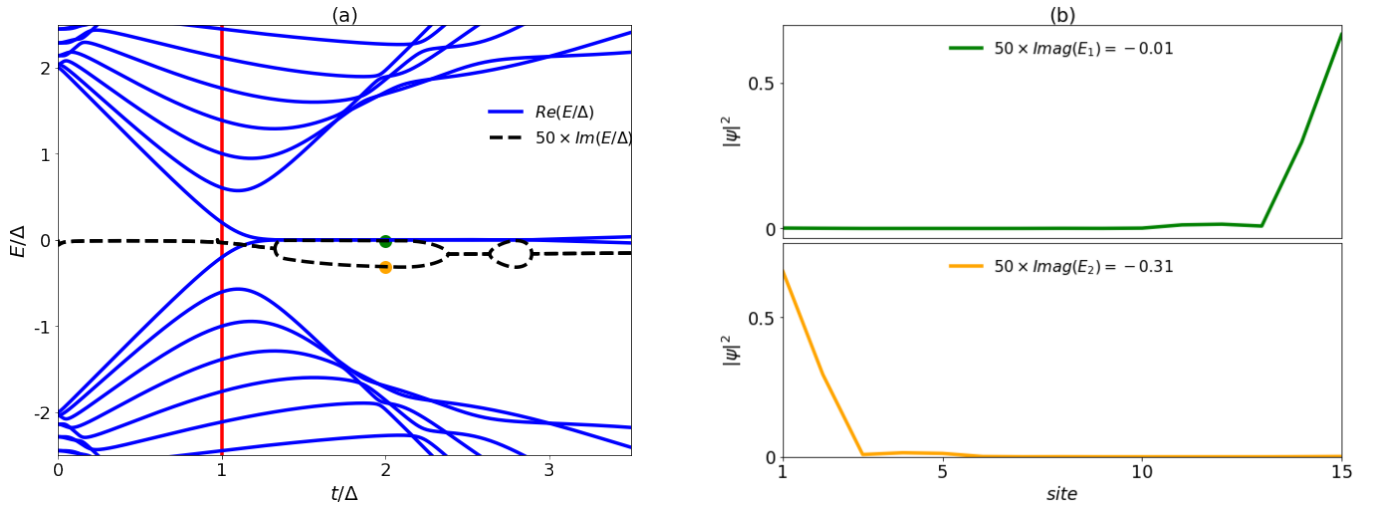


FIG. S7. (a) Spectra of a non-Hermitian Hamiltonian of a Kitaev chain coupled to external leads $H_{eff} = H_K + \Sigma$, using $N = 15$, $\mu/\Delta = 2$, $\Gamma_L = 5\epsilon_m$, $\gamma_0 = 190\epsilon_m$, and $\nu = 0.95$. Note that whenever the energy is smaller than a certain threshold, there is a bifurcation of the imaginary part of the lowest mode and its particle-hole partner (E_1 and E_2) (b) Probability densities for the two lowest modes for $t/\Delta = 2$ indicated by the green and orange dots in (a). The left Majorana (orange) leaks to the lead due to a larger value of its imaginary part, while the right Majorana (green) has a significantly larger lifetime.

- [2] R. Hess, H. F. Legg, D. Loss, and J. Klinovaja, Phys. Rev. B **104**, 075405 (2021).
- [3] E. Prada, P. San-Jose, and R. Aguado, Phys. Rev. B **86**, 180503 (2012).
- [4] S. D. Sarma, J. D. Sau, and T. D. Stanescu, Phys. Rev. B **86**, 220506 (2012).
- [5] D. Rainis, L. Trifunovic, J. Klinovaja, and D. Loss, Phys. Rev. B **87**, 024515 (2013).
- [6] J. Nilsson, A. Akhmerov, and C. Beenakker, Phys. Rev. Lett. **101**, 120403 (2008).
- [7] K. Flensberg, Physical review letters **106**, 090503 (2011).
- [8] L. Fu, Phys. Rev. Lett. **104**, 056402 (2010).
- [9] J. J. He, T. K. Ng, P. A. Lee, and K. T. Law, Phys. Rev. Lett. **112**, 037001 (2014).
- [10] J. Danon, A. B. Hellens, E. B. Hansen, L. Casparis, A. P. Higginbotham, and K. Flensberg, Phys. Rev. Lett. **124**, 036801 (2020).
- [11] G. Blonder, m. M. Tinkham, and k. T. Klapwijk, Phys. Rev. B **25**, 4515 (1982).
- [12] K. Flensberg, Phys. Rev. B **82**, 180516 (2010).
- [13] W. Heiss, J. Phys. A: Math. Theor. **45**, 444016 (2012).
- [14] J. Avila, F. Peñaranda, E. Prada, P. San-Jose, and R. Aguado, Communications Physics **2**, 1 (2019).